Computationally driven high-throughput identification of CaTe and Li_3Sb as promising candidates for high-mobility *p*-type transparent conducting materials

Viet-Anh Ha, Guodong Yu,* Francesco Ricci, Diana Dahliah, Michiel J. van Setten,† Matteo Giantomassi, Gian-Marco Rignanese, and Geoffroy Hautier‡

Institute of Condensed Matter and Nanoscience (IMCN), Université catholique de Louvain (UCLouvain), Chemin étoiles 8, bte L7.03.01, Louvain-la-Neuve 1348, Belgium

(Received 12 November 2018; published 4 March 2019)

High-performance *p*-type transparent conducting materials (TCMs) must exhibit a rare combination of properties including high mobility, transparency, and *p*-type dopability. The development of high-mobility/conductivity *p*-type TCMs is necessary for many applications such as solar cells or transparent electronic devices. Oxides have been traditionally considered as the most promising chemical space to dig out novel *p*-type TCMs. However, nonoxides might perform better than traditional *p*-type TCMs (oxides) in terms of mobility. We report on a high-throughput computational search for nonoxide *p*-type TCMs from a large data set of more than 30 000 compounds which identified CaTe and Li_3Sb as very good candidates for high-mobility *p*-type TCMs. From our calculations, both compounds are expected to be *p*-type dopable: intrinsically for Li_3Sb while CaTe would require extrinsic doping. Using electron-phonon computations, we estimate hole mobilities at room temperature to be about 20 and 70 $cm^2/V\,s$ for CaTe and Li_3Sb, respectively. These are "upper bound" values as only scattering with phonons is taken into account. The computed hole mobility for Li_3Sb is quite exceptional and comparable with the electron mobility in the best *n*-type TCMs.

DOI: 10.1103/PhysRevMaterials.3.034601

I. INTRODUCTION

Transparent conducting materials (TCMs) are necessary in many applications ranging from solar cells to transparent electronics. So far, *n*-type oxides (e.g., In_2O_3, SnO_2, and ZnO) are the highest-performing TCMs, allowing them to be used in commercial devices [1–5]. On the other hand, *p*-type TCMs show poorer performances, especially in terms of carrier mobility. This hinders the development of new technologies such as transparent solar cells or transistors [3,6]. Taking advantage of the predictive power of density functional theory (DFT) calculations, we have set up a high-throughput (HT) computational framework to identify novel *p*-type TCMs focusing first on oxide compounds [7–9].

The analysis of the calculated HT data confirmed that on average *p*-type oxides have inherently higher effective masses than *n*-type oxides [7]. This could be traced back to the strong oxygen *p*-orbital character in the valence band of most oxides and has rationalized the current gap in mobility between the best *p*-type and *n*-type oxides. This inherent difficulty in developing high-hole-mobility oxides justifies moving towards nonoxide TCM chemistries including fluorides [10], sulfides [11,12], oxianions [13], or germanides [14]. Recently, we started extending our HT computing approach to search for nonoxide TCMs. Phosphides were identified to be among the lowest hole effective mass materials and more specifically boron phosphide (BP) was detected as a very promising *p*-type TCM candidate [15]. We note that subsequent computational studies focusing on selected binaries and ternaries reported also on the computational screening of nonoxide TCMs [16,17]. In the present work, we extend our HT computing approach to a larger space of chemistries and investigate some selected candidates. We screen all nonoxide compounds in a large computational data set including more than 34 000 compounds with fundamental band gaps (computed by DFT) > 0 eV [18]. Combining DFT-based HT computations with higher-accuracy methods such as *GW*, hybrid functionals, and electron-phonon coupling computations (to assess the relaxation time and thus the mobility), we identify that CaTe and Li_3Sb would be of great interest as high-mobility *p*-type TCMs.

II. METHODS

All the considered materials originate from the Inorganic Crystal Structure Database (ICSD) [19]. Their relaxed crystal structures and electronic band structures were obtained from the Materials Project database [20,21]. These rely on DFT high-throughput computations which were performed with VASP [22,23] using the Perdew-Burke-Ernzerhof (PBE) exchange-correlation (XC) functional [24] within the projector augmented wave (PAW) framework [25].

One of the first selection criteria for TCMs is their stability. Here, it is assessed by the energy above hull E_{hull} in the Materials Project database [20]. For a compound stable at 0 K, $E_{hull} = 0$ meV/atom, and the stability decreases as E_{hull} increases.

*Present address: School of Physics and Technology (SPT), Wuhan University (WHU), Wuhan 430072, China.
†Present address: IMEC, 75 Kapeldreef, B-3001 Leuven, Belgium.
‡geoffroy.hautier@uclouvain.be

In the beginning of the screening procedure, the PBE band gap can be used as a filter. However, since PBE is known to systematically underestimate the band gap compared to experiments, more accurate calculations are needed in the subsequent steps (though with a limited number of materials). So, the fundamental and direct band gaps were also calculated with VASP for about a hundred materials using the Heyd-Scuseria-Ernzerhof (HSE) hybrid XC functional [26,27] and adopting the same computational parameters as for the PBE calculations. For the final candidates (CaTe and Li_3Sb), G_0W_0 calculations were performed with ABINIT [28–31]. In these calculations, optimized norm-conserving (NC) pseudopotentials including semicore electrons were used which were generated with ONCVPSP [32,33]. The kinetic cutoff energy for the wave functions was set to 51 and 52 Ha for CaTe and Li_3Sb, respectively, as recommended in the PseudoDojo table [33]. The convergence of these calculations with respect to the kinetic energy cutoff E_c for the dielectric function and the number of bands N_b was tested using automatic *GW* workflows [34] based on the PYMATGEN [35] and ABIPY packages [31,36]. For CaTe, the convergence of the gap at the Γ point (with a truncation error smaller than 0.01 eV) was obtained for $E_c = 12$ Ha and $N_b = 480$. In the case of Li_3Sb, the convergence is significantly faster: using $E_c = 10$ Ha and $N_b = 240$ guarantee a truncation error smaller than 0.01 eV. More details about the convergence tests are available in the Supplemental Material [51]. For the calculations of the screening and the quasiparticle self-energy, $10 \times 10 \times 10$ and $8 \times 8 \times 8$ **k**-point meshes were used for CaTe and Li_3Sb, respectively. The band structures are then interpolated from these **k**-point meshes using ABIPY [31,36].

The point defect computations were performed using the supercell technique [37] adopting $3 \times 3 \times 3$ supercells of the primitive cells. We calculated the defect formation energies first using the PBE XC functional but also with the more accurate HSE functional for Li_3Sb and CaTe [26,27]. For the latter, the screening length and fraction of exact exchange were set to the common values of 0.2 Å and 25%, respectively. The kinetic energy cutoff for the wave functions was set to 19.1 Ha (520 eV) and the relaxations are stopped when the change in total energy between two ionic relaxation-steps is smaller than 3.67×10^{-4} Ha (0.01 eV). The formation energy of defect D in charged state q can be written as [38,39]

$$E_f[D^q] = E[D^q] + E_{\text{corr}}[D^q] - E[bulk] - \Sigma_i n_i \mu_i + q(\epsilon_{\text{VBM}} + \Delta v + \Delta\epsilon_F), \quad (1)$$

where $E[D^q]$ and $E[bulk]$ are the total energies of the supercell with a defect D in the charge state q and without any defects, respectively; n_i is the number of atoms of type i removed ($n_i < 0$) or added ($n_i > 0$); and, μ_i is the corresponding chemical potential. ϵ_{VBM} is the energy of the valence band maximum (VBM), and $\Delta\epsilon_F$ is the Fermi level referenced to ϵ_{VBM}. The correction terms $E_{\text{corr}}[D^q]$ and Δv are introduced to take care of the spurious image-charge interactions and the potential alignment for charged defects, respectively. The defect states with the charge q were corrected using the extended Freysoldt (Kumagai) scheme [40,41]. All defects computations were performed using the PyCDT package [42].

The effective masses were calculated with BoltzTrap (based on Boltzmann transport theory framework) [43] using the PYMATGEN [35] interface and the Fireworks workflow package [44]. All the raw effective mass data are freely available in a separate paper which covers around 48 000 inorganic materials [18]. The mobility depends on the effective mass m^* through $\mu = e\tau/m^*$ where the relaxation time τ (inverse of the scattering rate) depends on different scattering mechanisms. Carriers can be scattered by phonons, ionized and neutral impurities, grain boundaries, etc. In this work, we only took into account the scattering of electrons by phonons which is likely to be an important component of scattering and is an intrinsic mechanism, difficult to control through purity and microstructure. The carrier scattering by phonons can be computed theoretically if the electron-phonon matrix elements are known. In principle, one can employ density functional perturbation theory (DFPT) to obtain all the electron-phonon matrix elements from first principles. However, converging the relevant physical properties (such as the scattering rate of electrons by phonons) often requires very dense **k**-point and **q**-point meshes for electrons and phonons, respectively, leading to a considerable increase of computational time. The recently developed interpolation techniques based on Wannier functions offer a very practical and efficient solution to overcome this obstacle. In this work, we used the EPW code [45,46] interfaced with Quantum ESPRESSO [47,48] to calculate the relaxation time $\tau_{n\mathbf{k}}$ (n and **k** are the band index and wave vector of a Bloch state, respectively). More details on the theory and the implementation can be found in Ref. [46]. The $\tau_{n,\mathbf{k}}$ were interpolated on a dense $40 \times 40 \times 40$ mesh for both **k** points (for electrons) and **q** points (for phonons) starting from the DFPT values on a $6 \times 6 \times 6$ mesh. The latter (together with the structural relaxation, self-consistent, and non-self-consistent calculations which are needed to run EPW) were obtained using Quantum ESPRESSO with NC pseudopotentials and very stringent parameters for convergence, e.g., a high cutoff energy of 40 Ha. These $\tau_{n,\mathbf{k}}$ are then used as an input to compute the carrier mobility by solving the Boltzmann transport equation by means of the BoltzTrap package [43]. In the latter calculations, the DFT band energies (computed on a finite number of **k** points) are interpolated using star functions (see Sec. 2 of Ref. [43]). Here, we have implemented another interpolation for the relaxation time in BoltzTrap in order to obtain the same very dense **k**-point grid as the one used for band energies. The physical principle for this implementation is that the symmetries of the quasiparticle energies are the same as those of band energies [49] ($\tau_{n,\mathbf{k}}$ due to the interaction with phonons can be calculated from the imaginary part of the electron-phonon self-energy).

III. RESULTS

Starting from the Materials Project database, our first step was to extract materials with a low hole effective mass ($<1\,m_o$, where m_o is the free electron mass) and a large enough fundamental gap (>0.5 eV) and direct gap (>1.5 eV), based on PBE calculations. Regarding the effective masses, in the most general form, they are represented by a tensor. As most TCMs are used as polycrystalline films, materials

TABLE I. Formula, space group, Materials Project identification number (MP-id) [20,21], fundamental E_g and direct gaps E_g^d computed by HSE functional (in eV), energy above hull E_{hull} (in meV/atom), principal components m_1, m_2, and m_3 of the hole effective mass tensor (in atomic units), and verification of the absence of toxic/rare-earth (T/RE) elements (Be, As, Cd, Yb, Hg, Pb, and Th) and of the *p*-type dopability (when computed here or obtained from the existing literature) for the selected compounds (see text). The materials are sorted as a function of the direct band gap in decreasing order.

Formula	Space group	MP-id	E_g^d	E_g	E_{hull}	m_1	m_2	m_3	T/RE	*p* dopability
BeS	$F\bar{4}3m$	422	6.89	4.05	0.0	0.65	0.65	0.65	×	
KM_gH_3	$Pm\bar{3}m$	23737	5.76	3.58	0.0	0.75	0.75	0.75	✓	
SiC	$F\bar{4}3m$	8062	5.75	2.25	0.7	0.58	0.58	0.58	✓	✓ [52–55]
BeSe	$F\bar{4}3m$	1541	5.27	3.36	0.0	0.55	0.55	0.55	×	
$BeCN_2$	$I\bar{4}2d$	15703	5.21	5.21	0.0	0.75	0.75	0.78	×	
$RbPbF_3$	Cc	674508	5.20	4.84	0.0	0.71	0.83	0.95	×	
MgS	$Fm\bar{3}m$	1315	4.95	3.84	0.0	0.98	0.98	0.98	✓	
$RbHgF_3$	$Pm\bar{3}m$	7482	4.90	2.11	0.0	0.93	0.93	0.93	×	
AgCl	$Fm\bar{3}m$	22922	4.81	2.28	0.0	0.83	0.83	0.83	✓	
$CsHgF_3$	$Pm\bar{3}m$	561947	4.59	2.20	0.0	0.89	0.89	0.89	×	
Be_2C	$Fm\bar{3}m$	1569	4.56	1.63	0.0	0.37	0.37	0.37	×	
$SrMgH_4$	$Cmc2_1$	643009	4.52	3.78	0.0	0.84	0.90	0.95	✓	
Li_2Se	$Fm\bar{3}m$	2286	4.36	3.70	0.0	0.95	0.95	0.95	✓	
BP	$F\bar{4}3m$	1479	4.35	2.26	0.0	0.34	0.34	0.34	✓	✓ [15]
CaS	$Fm\bar{3}m$	1672	4.28	3.34	0.0	0.88	0.88	0.88	✓	
$LiCa_4B_3N_6$	$Im\bar{3}m$	6799	4.25	3.38	0.0	0.86	0.86	0.86	✓	
$BaSrI_4$	$R\bar{3}m$	754852	4.22	4.22	21.8	0.73	0.73	0.80	✓	
$LiSr_4B_3N_6$	$Im\bar{3}m$	9723	4.18	3.22	0.0	0.89	0.89	0.89	✓	
$NaSr_4B_3N_6$	$Im\bar{3}m$	10811	4.08	3.14	0.0	0.92	0.92	0.92	✓	
K_2LiAlH_6	$Fm\bar{3}m$	24411	4.04	3.70	9.1	0.65	0.65	0.65	✓	
BeTe	$F\bar{4}3m$	252	4.04	2.45	0.0	0.42	0.42	0.42	×	
Ba_3SrI_8	$I4/mmm$	756235	4.02	4.02	7.5	0.70	0.81	0.81	✓	
CaSe	$Fm\bar{3}m$	1415	4.01	2.95	0.0	0.77	0.77	0.77	✓	
LiH	$Fm\bar{3}m$	23703	3.97	3.97	0.0	0.46	0.46	0.46	✓	×
AlP	$F\bar{4}3m$	1550	3.90	2.50	0.0	0.56	0.56	0.56	✓	×
YbS	$Fm\bar{3}m$	1820	3.76	2.96	0.0	0.76	0.76	0.76	×	
Na_2LiAlH_6	$Fm\bar{3}m$	644092	3.75	3.75	3.9	0.66	0.66	0.66	✓	
SrSe	$Fm\bar{3}m$	2758	3.68	3.03	0.0	0.83	0.83	0.83	✓	
$BaLiH_3$	$Pm\bar{3}m$	23818	3.62	3.26	0.0	0.36	0.36	0.36	✓	×
$CsPbF_3$	$Pm\bar{3}m$	5811	3.59	3.59	4.6	0.39	0.39	0.39	×	
Cs_3ZnH_5	$I4/mcm$	643702	3.58	3.58	0.0	0.69	0.93	0.93	✓	
Al_2CdS_4	$Fd\bar{3}m$	9993	3.56	3.55	20.0	0.78	0.78	0.78	×	
K_2LiAlH_6	$R\bar{3}m$	23774	3.52	3.52	0.0	0.68	0.84	0.84	✓	
$BaMgH_4$	$Cmcm$	643718	3.51	3.26	4.8	0.48	0.55	0.70	✓	
CaTe	$Fm\bar{3}m$	1519	3.50	2.18	0.0	0.60	0.60	0.60	✓	✓
Cs_3MgH_5	$P4/ncc$	23947	3.49	3.49	0.3	0.88	0.93	0.93	✓	
Cs_3MgH_5	$I4/mcm$	643895	3.49	3.49	0.0	0.83	0.94	0.94	✓	
YbSe	$Fm\bar{3}m$	286	3.48	2.43	0.0	0.67	0.67	0.67	×	
ZnS	$F\bar{4}3m$	10695	3.46	3.46	0.0	0.81	0.81	0.81	✓	✓ [12]
$TaCu_3S_4$	$P\bar{4}3m$	10748	3.46	2.95	0.0	0.98	0.98	0.98	✓	
Al_2ZnS_4	$Fd\bar{3}m$	4842	3.46	3.43	0.0	0.66	0.66	0.66	✓	×
Li_2ThN_2	$P\bar{3}m1$	27487	3.46	3.33	0.0	0.85	0.95	0.95	×	
$Mg_2B_{24}C$	$P\bar{4}n2$	568556	3.42	3.41	0.0	0.77	0.93	0.93	✓	
Li_2GePbS_4	$I\bar{4}2m$	19896	3.33	3.20	0.0	0.61	0.61	0.98	×	
Cs_3H_5Pd	$P4/mbm$	643006	3.32	3.09	0.0	0.79	0.83	0.83	✓	
SrTe	$Fm\bar{3}m$	1958	3.24	2.39	0.0	0.67	0.67	0.67	✓	×
MgTe	$F\bar{4}3m$	13033	3.24	3.24	0.9	0.95	0.95	0.95	✓	
$CsTaN_2$	$I\bar{4}2d$	34293	3.22	3.22	0.0	0.71	0.71	0.92	✓	
Cs_3MnH_5	$I4/mcm$	643706	3.21	3.18	0.0	0.82	0.96	0.96	✓	
LiMgP	$F\bar{4}3m$	36111	3.18	2.00	0.0	0.65	0.65	0.65	✓	
BaS	$Fm\bar{3}m$	1500	3.17	3.02	0.0	0.85	0.85	0.85	✓	
$LiAlTe_2$	$I\bar{4}2d$	4586	3.11	3.11	0.0	0.52	0.83	0.83	✓	
YbTe	$Fm\bar{3}m$	1779	3.09	1.76	0.0	0.54	0.54	0.54	×	

TABLE I. *(Continued.)*

Formula	Space group	MP-id	E_g^d	E_g	E_{hull}	m_1	m_2	m_3	T/RE	p dopability
Li_3Sb	$Fm\bar{3}m$	2074	3.06	1.15	0.0	0.24	0.24	0.24	✓	✓
$SrAl_2Te_4$	$I422$	37091	3.06	2.66	0.0	0.42	0.79	0.80	✓	
$TaCu_3Te_4$	$P\bar{4}3m$	9295	3.05	2.50	0.0	0.63	0.63	0.63	✓	
$CsPbCl_3$	$Amm2$	675524	2.99	2.99	0.0	0.30	0.32	0.33	×	
$TaCu_3Se_4$	$P\bar{4}3m$	4081	2.98	2.43	0.0	0.82	0.82	0.82	✓	
BaSe	$Fm\bar{3}m$	1253	2.95	2.59	0.0	0.76	0.76	0.76	✓	
KAg_2PS_4	$I\bar{4}2m$	12532	2.87	2.53	0.0	0.67	0.82	0.82	✓	
AlAs	$F\bar{4}3m$	2172	2.84	2.12	0.0	0.50	0.50	0.50	×	
$LiErS_2$	$I4_1/amd$	35591	2.80	2.80	10.4	0.62	0.99	0.99	✓	
GaN	$F\bar{4}3m$	830	2.80	2.80	5.2	0.94	0.94	0.94	✓	

with isotropic or close to isotropic transport are easier to use in practical applications. Therefore, for the screening, we focus on the three principal values of this tensor and sort the materials based on the highest of the three principal hole effective masses. There were about 390 compounds passing through this first filter.

We then screened out very unstable materials selecting only those with an energy above hull lower than 24 meV/atom. This threshold corresponds to the typical standard deviation of computational errors (compared with experiment) of DFT formation energies [50]. For the 107 materials passing these criteria, more accurate fundamental and direct gaps were calculated using the HSE hybrid functional. All the results of this step are presented in Table SI of the Supplemental Material [51]. For sake of clarity, Table I shows a selection of 63 materials with a direct band gap $\geqslant$2.8 eV. The materials are sorted in decreasing order as a function of the computed direct band gap.

Among the materials at the top of the list, SiC is a well-known wide-band-gap semiconductor. This material exhibits polymorphism (e.g., cubic: 3C, rhombohedral: 15R, hexagonal: 6H, 4H, 2H) [56] and can be doped both n and p type [52–55]. A high hole mobility of 40 cm^2/V s was obtained for the cubic phase [57]. The indirect optical absorption of cubic phase is very weak at room temperature with a coefficient of 10^3 cm^{-1} at 3.1 eV [58]. We suggest that SiC can be considered as a good p-type TCM. The main disadvantage of this compound is the difficulty of hole doping. Most known impurities such as Al, B, Ga, and Sc create deep doping levels leading to rather low concentrations of holes which were typically measured to be lower than 10^{18} cm^{-3} [57] and are suitable for transistor applications.

Next comes a series of beryllium-based compounds (BeS, BeSe, $BeCN_2$, Be_2C, and BeTe). While their computed performance in terms of band gap and hole effective masses is very attractive, the toxicity of beryllium lowers their interest for technological applications. Likewise, the many lead-based halide perovskites ($CsPbCl_3$, $RbPbF_3$, and $CsPbF_3$) and Li_2GePbS_4 also present toxicity issues. It is interesting however to see these halide perovskites being of great interest as solar absorbers when they are made in chemistries showing smaller gaps [59,60]. Toxicity is also an issue with the series of arsenides, e.g., AlAs. These arsenides are also very analogous to the phosphides such as BP and AlP that were identified in a previous work [15]. Some of the materials in the list contain rare-earth elements which might present some cost issues. We believe that further assessment of all these materials in terms of dopability and mobility is not a priority. Therefore, in the penultimate column of Table I, the absence of toxic or rare-earth elements is verified, as indicated by a check mark.

Continuing to explore the list of materials, many hydrides appear to be of interest with low hole effective mass and large direct band gaps for LiH, $BaLiH_3$, and CsH. Unfortunately, our subsequent defect computations indicate that these hydrides have low-lying hole-killing defects, especially the hydrogen vacancy, making unlikely their efficient p-type doping (see the Supplemental Material [51]). A few sulfides are also identified by our screening: ZnS and $ZnAl_2S_4$. ZnS has been indeed recently studied as a good-performance p-type TCM [12]. $ZnAl_2S_4$, on the other hand, is less studied but our defect computation indicates that it is very unlikely to be p-type dopable because Zn-Al antisite defects form easily and act as hole killers. Al_2CdS_4 is likely to present the same issues. The defect formation energies computed by DFT for $ZnAl_2S_4$ are given in the Supplemental Material [51].

Among the different materials in the table, two promising candidates, Li_3Sb and CaTe, also attracted our attention. The rest of the paper is dedicated to the further computations that were performed for these compounds.

The conventional cells of CaTe and Li_3Sb are shown in Figs. 1(a) and 1(e). Ca atoms in CaTe are surrounded by six Te atoms forming an octahedral local environment. In Li_3Sb, the cation fills tetrahedral and octahedral sites. Both CaTe and Li_3Sb are cubic phases with high symmetry, which explains their isotropy in hole effective masses ($m_1 = m_2 = m_3$). CaTe and Li_3Sb exhibit very low hole effective masses with the eigenvalues being 0.60 and 0.25 m_o (m_o is the mass of a free electron), respectively. It is worth noting that the lowest hole effective masses found so far in a computational database for a p-type conducting oxide, $K_2Sn_2O_3$ [7,61], is 0.27 m_o. The promising nonoxide p-type TCM reported recently [15], BP, shows an effective mass around 0.35 m_o. Current Cu-based p-type transparent conducting oxides (TCOs) show effective masses around 1.5 to 2 m_o [7]. The direct gaps of CaTe and Li_3Sb calculated using the HSE hybrid functional are 3.5 and 3.06 eV, respectively. Next to hybrid functional computations, we performed G_0W_0 to confirm the value of these band gaps.

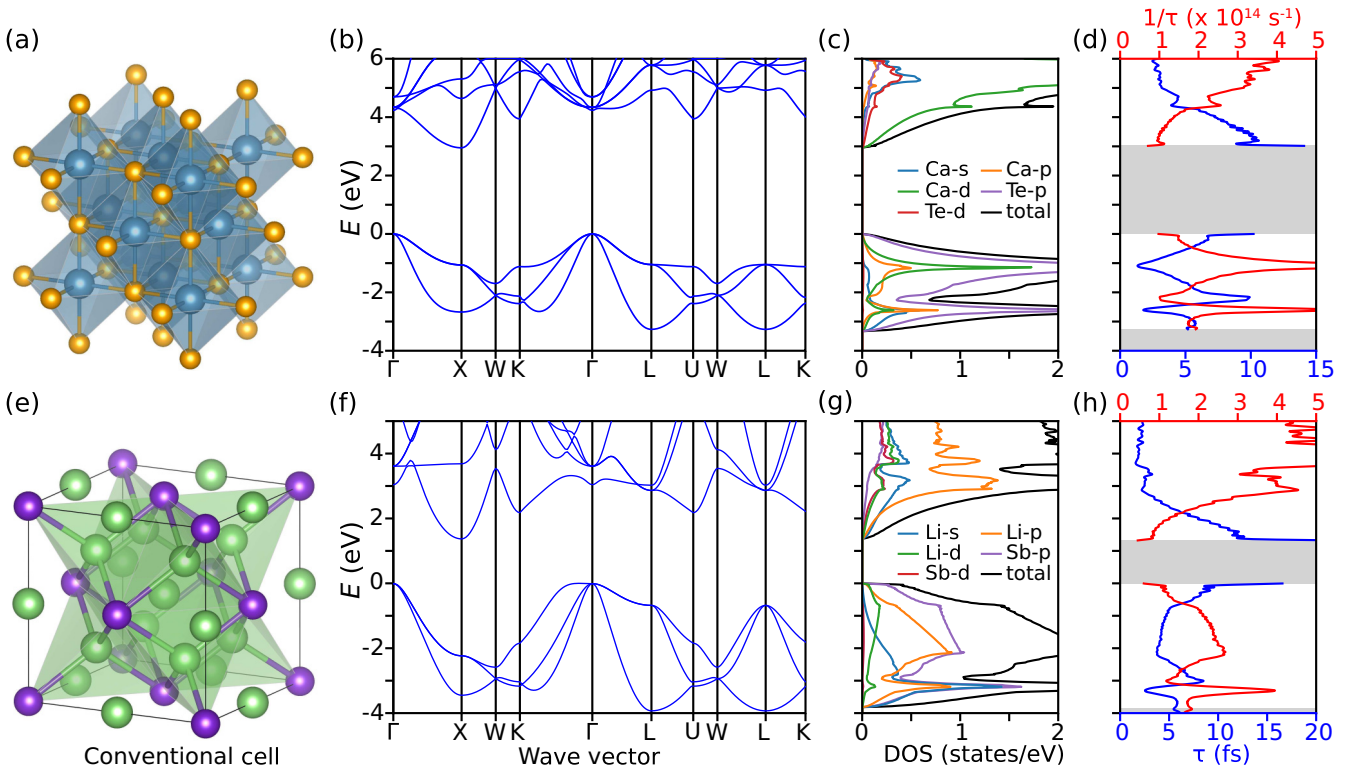

FIG. 1. From the left to the right, the conventional cells, band structures, projected density of states (DOS), and relaxation time and scattering rate. Panels (a)–(d) and (e)–(h) show data of CaTe and Li_3Sb, respectively. The conventional cells present local environments around cations Ca (blue) and Li (green). Panels (b) and (f) plot DFT band structures with a rigid shift of the conduction bands (scissor operator) to fit the fundamental gaps computed by G_0W_0. Panels (d) and (h) show relaxation time τ (in femtoseconds) and scattering rate $1/\tau$ (in 1/second) as functions of energy at temperature 300 K. The projected DOS in (c) and (g) are computed by DFT. The band gaps of the DOS and relaxation time are also shifted to fit G_0W_0 values.

Figure 1(b) shows the DFT band structure with a scissor shift to fit the G_0W_0 fundamental gap (G_0W_0 band structure of CaTe is shown in Fig. S6 of the Supplemental Material [51]). The G_0W_0 fundamental gap ($\Gamma - X$) is 2.95 eV while the direct gap is located at the X point and has a value of 4.14 eV. The G_0W_0 direct gap is consistent with the value of 4.1 eV measured in an optical experiment [62]. We expect such a large direct band gap to lead to transparency in the visible region. Li_3Sb is also a semiconductor with an indirect gap. In the same way, the DFT electronic band structure with a scissor shift is presented in Fig. 1(f) (see Fig. S7 of the Supplemental Material [51] for G_0W_0 band structure). The G_0W_0 fundamental (indirect) band gap and direct gap are 1.37 and 3.17 eV, respectively. The G_0W_0 direct gap (located at the Γ point) is 3.17 eV. This is consistent with an experimental value of 3.1 eV measured recently [63] but much lower than another experimental value of 3.9 eV reported earlier [64]. The indirect band gap is narrow and will lead to some absorption in the visible range. However, the indirect nature of the absorption makes it phonon-assisted and is expected to lead to weak absorption. To quantify this absorption, we computed the optical absorption including phonon-assisted processes using EPW [45,46]. Details about the computational method can be found in Ref. [65]. The result in Fig. 2 shows quite weak absorption in the visible range with the average intensity about 5×10^3 cm^{-1}, which means that a 100-nm film still allows more than 70% of visible light energy to get through. This is suitable for applications and devices using the thin-film form of Li_3Sb. The weak indirect optical absorption computed here is similar to that of established p-type TCOs such as SnO [66] or recently proposed p-type TCMs such as BP [15].

CaTe and Li_3Sb show very low hole effective mass (0.60 and 0.24 m_o within DFT). Indeed, both materials have

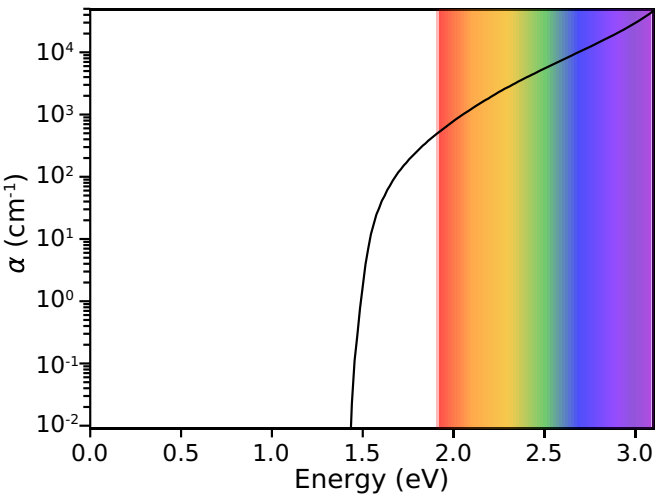

FIG. 2. The indirect optical absorption of Li_3Sb due to phonon-assisted transitions.

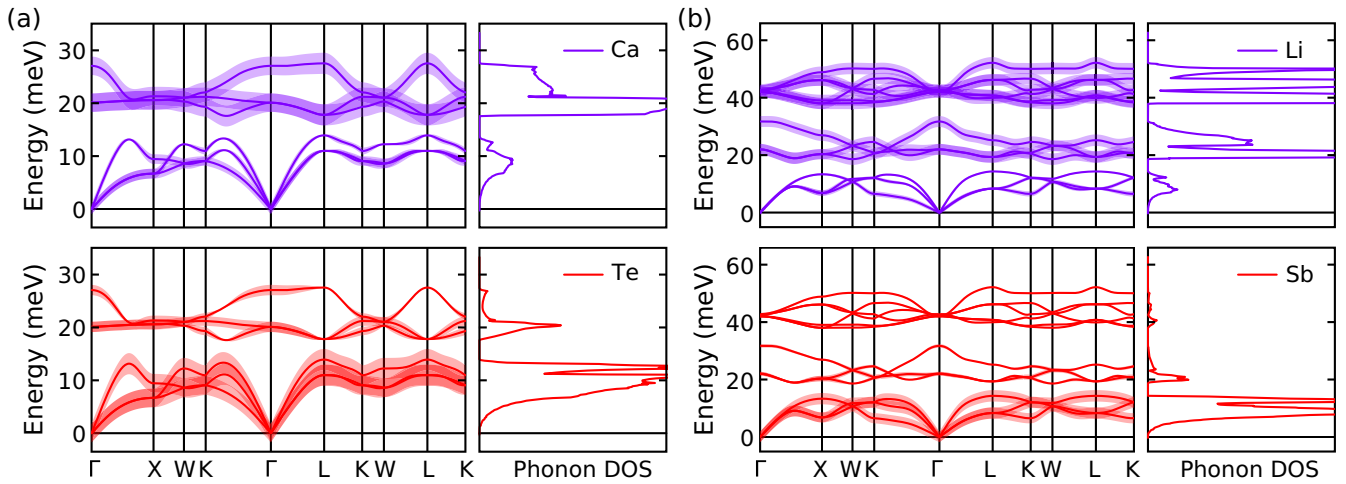

FIG. 3. Phonon band structures with fat bands representing displacements of atomic vibrations. The width of fat bands gives qualitative understanding of the vibrational modes such as what are the atomic types involved in the vibrations at a given energy, their direction of oscillation, and the amplitude (related to the displacement). The projected DOS of phonons on each type of atom are correspondingly shown next to the band structures. (a) CaTe and (b) Li_3Sb.

threefold degeneracy at VBM (Γ point); therefore, the transport of holes occurs in three bands with some lighter and some heavier. Our definition of effective mass takes into account the competition among these three bands and gives an average value that is representative of the transport which will happen in the different bands. More details about formulas and calculation techniques can be found in Refs. [18,67]. This should be kept in mind when comparing our results to other studies which sometimes only focus on one band when several competing bands are present [16,68]. It is worth noting that the effective masses might be changed in the *GW* band structures, which is not assessed in this work. Here, we still use the DFT band structures for the transport calculations. Figure 1 shows the projected density of states (DOS) for [panel (c)] CaTe and [panel (g)] Li_3Sb. For both compounds, the top of the valence band is mainly of anionic *p*-orbital character (Sb^{3-} or Te^{2-}) with some mixing from the cations. The effective masses are directly related to overlap and energy difference between orbitals [67]. The lower value of hole effective masses obtained in these nonoxide compounds can be associated with both a better alignment between the anionic and cationic states than in oxides and larger anionic *p* orbitals ($5p$ versus $2p$ for oxides).

The effective mass is an important factor driving carrier mobility but not the only one. The scattering rate or relaxation time also affects the mobility. There are several mechanisms which can influence relaxation time as mentioned in Sec. II. Phonon scattering is the most intrinsic factor as it is not affected by purity and microstructure. The evaluation of relaxation time from phonon scattering can be performed *ab initio* using electron-phonon coupling matrices obtained from DFPT phonon computations. Figure 3 shows phonon band structures (fat bands) and projected DOS of phonons for [panel (a)] CaTe and [panel (b)] Li_3Sb. The fat bands represent qualitatively characteristics of vibrational modes including what types of atoms participate in the phonon modes at a given energy and their direction and amplitude. The absence of modes with negative (purely imaginary) frequencies shows that these materials are dynamically stable at 0 K. The lighter atoms (Ca and Li) mainly contribute to the optical modes at high frequencies (3 and 9 modes in CaTe and Li_3Sb, respectively), while the heavier elements (Te and Sb) play an important role in the three acoustic modes at low frequencies.

Using the DFPT phonon computations and EPW, we can extract electron-phonon coupling matrices and the relaxation time τ_{nk} on a dense **k**-point grid (see Eq. S1 of the Supplemental Material [51]). Figures 1(d) and 1(h) show the scattering rate and lifetime (inverse of scattering rate) as a function of energy at 300 K for CaTe and Li_3Sb, respectively (see Eq. S2 of the Supplemental Material [51]). As commonly observed, the scattering rate is proportional to the DOS. A higher DOS offers more states available for the scattered electrons. At the doping hole concentration of 10^{18} cm^{-3}, the Fermi levels are 90.5 and 120.8 meV above the VBMs for CaTe and Li_3Sb, respectively. For the highest doping of 10^{21} cm^{-3}, the Fermi levels lie below VBMs of 264.5 and 168.5 meV for CaTe and Li_3Sb, respectively. The transport of holes, therefore, takes place around VBMs (Γ points). The DOS at the Γ point of Li_3Sb is larger than that of CaTe but the scattering rate of Li_3Sb is fairly similar [see Figs. 1(d) and 1(h)], indicating that a slightly weaker electron-phonon coupling is present in Li_3Sb.

We computed scattering rates at temperatures of 300 and 400 K. Figure 4 shows the hole mobilities as a function of hole concentrations at 300 and 400 K for both CaTe and Li_3Sb. The mobilities decrease with hole concentrations. As the Fermi level shifts deeper below the VBMs, the DOS increases as well as the scattering rate [see Figs. 1(d) and 1(h)]. CaTe shows a value of hole mobility around 20 $cm^2/V\,s$ that is comparable with the mobility of Ba_2BiTaO_6, a recently reported *p*-type TCO [9], and larger than mobilities of the traditional *p*-type TCOs such as $CuAlO_2$ [69] and SnO [70]. Li_3Sb exhibits an exceptional hole mobility up to about 70 $cm^2/V\,s$ at room temperature. This value nearly reaches the values of the electron mobilities of the best current *n*-TCOs such as SnO_2, ZnO, In_2O_3, and Ga_2O_3 which are around 100 $cm^2/V\,s$

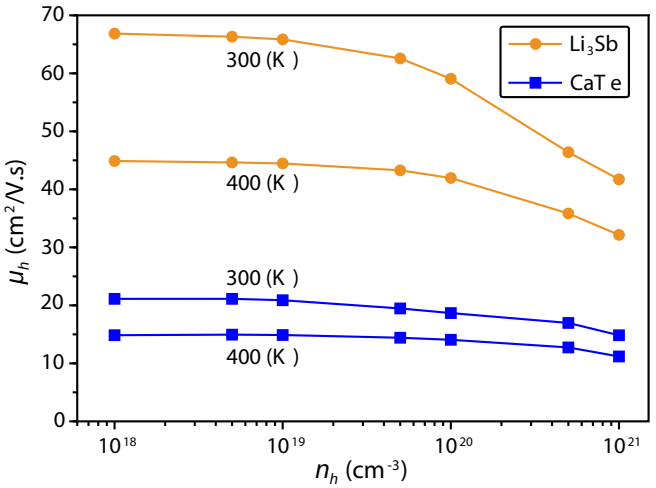

FIG. 4. Hole mobilities as a function of hole concentrations of CaTe and Li_3Sb at temperatures 300 and 400 K.

(see Table SII of the Supplemental Material [51]). It is worth noting that the mobility measured experimentally takes into account other scattering processes. Our computed mobilities as they only take into account phonon scattering can be seen as an upper bound.

Our final assessment focuses on the dopability of CaTe and Li_3Sb. While we have assumed so far that the Fermi level of these two materials could be tuned to generate hole carriers, it remains to be seen whether the defect chemistry is favorable to hole generation. To answer this question, we performed defect calculations using HSE functional following the procedure described in Sec. II. Figure 5(a) presents the defect formation energy for both intrinsic and extrinsic defects for each sort of defect in CaTe. The chemical potentials are chosen in conditions which lead to the most favorable *p*-type doping tendency for this material. The chemical potentials corresponding to different conditions in the phase diagrams are available in Fig. S8 of the Supplemental Material [51]. Focusing first on intrinsic defects only including vacancies, antisite defects (replacement of Te on Ca sites and vice versa), and interstitial atoms, defect formation energies of these are plotted in Fig. 5(a) with chemical potentials extracted in Te-rich condition of the phase diagram. Intrinsically, CaTe is unlikely to present *p*-type doping as no intrinsic defect acts as a low-lying acceptor. The vacancy of Ca will be in competition with the hole-killing vacancy of Te leading to a Fermi level far from the valence band. However, the Te vacancy is not low enough in energy that it would prevent extrinsic *p*-type doping. When extrinsic defects with Na, K, and Li substituting onto Ca sites are considered, we find that all these substitutions offer a shallow acceptor very competitive compared to the Te vacancy. The Ca by Na substitution is the lowest in energy. Extrinsic doping by Na might therefore lead to *p*-type doping in CaTe. The plots of formation energies of K_{Ca}, Na_{Ca}, and Li_{Ca} in Fig. 5(a) were achieved with chemical potentials extracted from KTe-CaTe-K_2Te_3, $NaTe_3$-CaTe-Na_2Te, and Li_2Te-CaTe-Te facets of the three-element phase diagrams (see Fig. S8 of the Supplemental Material [51]). For Li_3Sb, Fig. 5(b) shows an intrinsic tendency for hole doping with the lithium vacancy (Vac_{Li}) acting as a shallow acceptor with a very low formation energy and no competing hole killer.

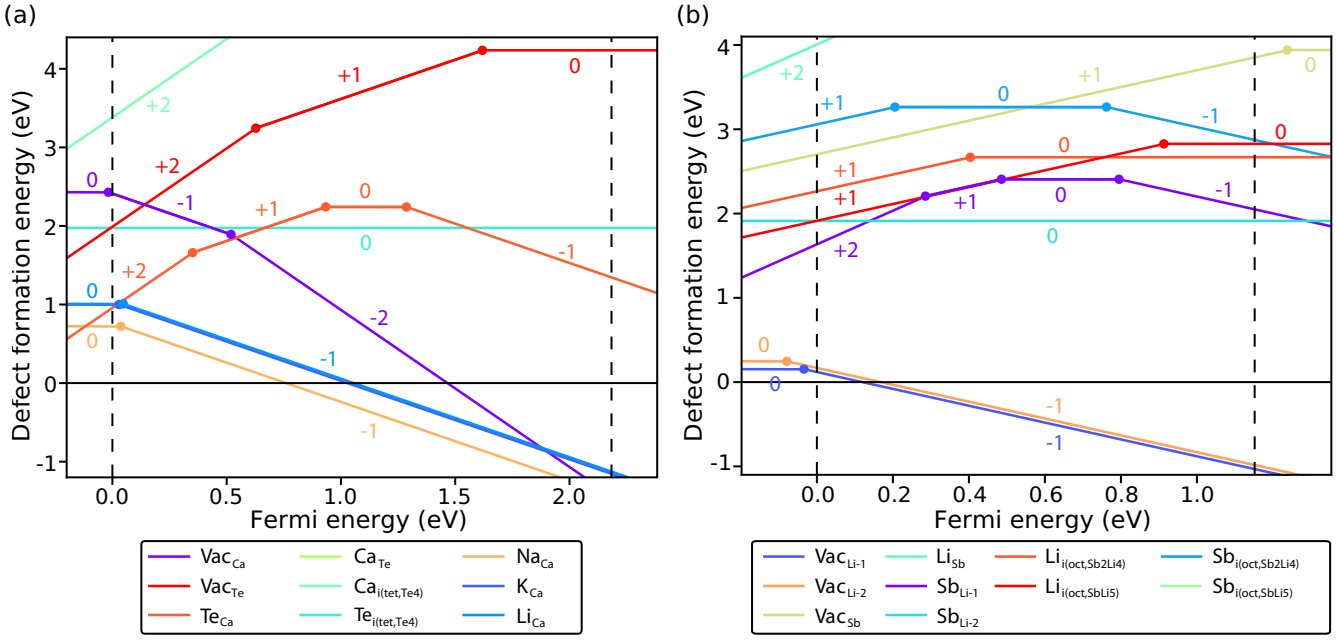

FIG. 5. The defect formation energy as a function of Fermi level of intrinsic and extrinsic defects for (a) CaTe and (b) Li_3Sb. For CaTe, the intrinsic defects include vacancies (Vac_{Ca} and Vac_{Te}), antisites (Te_{Ca} and Ca_{Te}), and interstitial atoms inserted into the tetrahedral hollows formed by 4 Te atoms ($Ca_{i(tet,Te4)}$ and $Te_{i(tet,Te4)}$), while Na, K, and Li are used as the extrinsic defects substituting Ca atoms (Na_{Ca}, K_{Ca}, and Li_{Ca}). For Li_3Sb, the intrinsic defects include vacancies ($Vac_{Li\text{-}1}$, $Vac_{Li\text{-}2}$, and Vac_{Sb}), antisites (Li_{Sb}, $Sb_{Li\text{-}1}$, and $Sb_{Li\text{-}2}$), and interstitial atoms inserted into the octahedral hollows formed by Sb and Li atoms ($Li_{i(oct,\ Sb2Li4)}$, $Li_{i(oct,\ SbLi5)}$, $Sb_{i(oct,\ Sb2Li4)}$, and $Sb_{i(oct,\ SbLi5)}$). In both cases, the VBM is set to zero.

This plot is produced with chemical potentials computed in the Li_3Sb-Li_2Sb facet of the phase diagram (see Fig. S9 of the Supplemental Material [51]).

IV. DISCUSSION

The discovery of the quite unanticipated Li_3Sb with a potential for very high hole mobility demonstrates the interest of our HT screening strategy. Li_3Sb is an unexpected compound for TCM applications and would have been difficult to intuitively identify. Among other A_3B compounds (A = Li, Na, K, and Rb; and B = N, P, As, and Sb), Li_3Sb is exceptional because of its very low hole effective masses (see Table SIII in the Supplemental Material [51]). We suggest that the energy difference between A-ns^1 ($n = 2, 3, 4, 5$ for Li, Na, K, and Rb, respectively) and B-np^3 ($n = 2, 3, 4, 5$ for N, P, As, and Sb, respectively) orbitals of valence electrons (A and B) might play important role here. In fact, the energy difference between Li-$2s^1$ and Sb-$5p^3$ is about 1.954 (eV) [33] and is the smallest value among many other ones of A-ns^1/B-np^3 pairs. This leads to a small orbital-energy difference and strong s/p (anti)bonding, which results in low hole effective mass. While we only focus on CaTe and Li_3Sb as they are likely the most potential candidates, there are other interesting materials with hole effective masses from 0.6 to 1.0 m_o and high direct gaps (see Table I) such as CaS, SrSe, SrTe, $LiCa_4B_3N_6$, $LiSr_4B_3N_6$, and $NaSr_4B_3N_6$. Defect calculations for these materials have not been performed in this work and we, therefore, cannot adjudge their p-type doping tendency.

By going beyond oxides, we identified compounds with very high hole mobility. However, several other issues also arise and need to be considered. The processing of antimonides or tellurides might be more difficult than oxides. They are, however, very common chemistries in other applications such as thermoelectrics with several exemplary compounds such as PbTe, Bi_2Te_3 [71], or more recently Mg_3Sb_2 [72–74]. The band gaps in nonoxide compounds are narrower, which lowers on average their transparency in the visible light. As we already discussed [15], this can be overcome by exploiting the indirect gaps and weak phonon-assisted optical transitions. Lower band gaps are useful for p dopability though as lower band gap materials tend to be easier to dope [75].

We note that the defect chemistry of nonoxides can be different than in traditional TCOs. For oxides, the cation-anion antisite defects (replacement of anions on cations' sites and vice versa) are unlikely to be favorable energetically because of the large electronegativity difference between cations and anions. In nonoxide compounds, e.g., CaTe, the cation-anion antisites are more likely to be present leading to potentially different hole-killing defects. While the anion (oxygen) vacancy is the most common hole killer in oxides, we see our nonoxide materials presenting antisite cation-anion defects lower in energy than the anion vacancy such as in CaTe. We also identify that the hydride chemistry while offering attractive electronic structures presents dopability issues (i.e., a low-lying hydrogen vacancy acting as hole killer) preventing them from further consideration in p-type TCMs.

V. CONCLUSIONS

Using a large database and appropriate filtering strategies, we report on a high-throughput search for nonoxide p-type TCMs. We identified two materials to be of interest: CaTe and Li_3Sb. We performed extensive follow-up computational investigation of these candidates, evaluating their band structure using beyond DFT techniques, their transport and phonon-assisted optical properties using electron-phonon computations, as well as their defect chemistry. Both CaTe and Li_3Sb present very attractive properties for p-type TCM applications. Li_3Sb shows a very high hole mobility of around 70 $cm^2/V\,s$, which is close to electron mobility in the best n-type TCMs. Our work motivates further experimental investigation of these two materials for TCM applications.

ACKNOWLEDGMENTS

V.-A.H. was funded through a grant from the FRIA. G.-M.R. is grateful to the F.R.S.-FNRS for financial support. G.H., G.-M.R., G.Y., and F.R. acknowledge the F.R.S.-FNRS project HTBaSE (Contract No. PDR-T.1071.15) for financial support. We acknowledge access to various computational resources: the Tier-1 supercomputer of the Fédération Wallonie-Bruxelles funded by the Walloon Region (Grant Agreement No. 1117545), and all the facilities provided by the Université catholique de Louvain (CISM/UCLouvain) and by the Consortium des Équipements de Calcul Intensif en Fédération Wallonie Bruxelles (CÉCI). The authors thank Dr. Samuel Poncé and Professor Emmanouil Kioupakis for helpful discussions on the technical aspects of the electron-phonon computations.

[1] H. Ohta and H. Hosono, Transparent oxide optoelectronics, Mater. Today **7**(6), 42 (2004).

[2] A. Facchetti and T. J. Marks (eds.), *Transparent Electronics: From Synthesis to Applications* (Wiley, Chichester, UK, 2010).

[3] K. Ellmer, Past achievements and future challenges in the development of optically transparent electrodes, Nat. Photonics **6**, 809 (2012).

[4] P. Barquinha, R. Martins, L. Pereira, and E. Fortunato, *Transparent Oxide Electronics: From Materials to Devices* (Wiley, Chichester, UK, 2012).

[5] E. Fortunato, P. Barquinha, and R. Martins, Oxide semiconductor thin-film transistors: A review of recent advances, Adv. Mater. **24**, 2945 (2012).

[6] S. C. Dixon, D. O. Scanlon, C. J. Carmalt, and I. P. Parkin, n-type doped transparent conducting binary oxides: An overview, J. Mater. Chem. C **4**, 6946 (2016).

[7] G. Hautier, A. Miglio, G. Ceder, G.-M. Rignanese, and X. Gonze, Identification and design principles of low hole effective mass p-type transparent conducting oxides, Nat. Commun. **4**, 2292 (2013).

[8] J. B. Varley, V. Lordi, A. Miglio, and G. Hautier, Electronic structure and defect properties of B_6O from hybrid functional and many-body perturbation theory calculations: A possible ambipolar transparent conductor, Phys. Rev. B **90**, 045205 (2014).

[9] A. Bhatia, G. Hautier, T. Nilgianskul, A. Miglio, J. Sun, H. J. Kim, K. H. Kim, S. Chen, G.-M. Rignanese, X. Gonze, and J. Suntivich, High-mobility bismuth-based transparent *p*-type oxide from high-throughput material screening, Chem. Mater. **28**, 30 (2016).

[10] H. Yanagi, J. Tate, S. Park, C.-H. Park, and D. Keszler, *p*-type conductivity in wide-band-gap BaCu*Q*F (Q = S, Se), Appl. Phys. Lett. **82**, 2814 (2003).

[11] S. Park, D. A. Keszler, M. M. Valencia, R. L. Hoffman, J. P. Bender, and J. F. Wager, Transparent *p*-type conducting $BaCu_2S_2$ films, Appl. Phys. Lett. **80**, 4393 (2002).

[12] R. Woods-Robinson, J. K. Cooper, X. Xu, L. T. Schelhas, V. L. Pool, A. Faghaninia, C. S. Lo, M. F. Toney, I. D. Sharp, and J. W. Ager, *p*-type transparent Cu-alloyed ZnS deposited at room temperature, Adv. Electron. Mater. **2**, 1500396 (2016).

[13] K. Ueda, S. Inoue, S. Hirose, H. Kawazoe, and H. Hosono, Transparent *p*-type semiconductor: LaCuOS layered oxysulfide, Appl. Phys. Lett. **77**, 2701 (2000).

[14] F. Yan, X. Zhang, Y. G. Yu, L. Yu, A. Nagaraja, T. O. Mason, and A. Zunger, Design and discovery of a novel half-Heusler transparent hole conductor made of all-metallic heavy elements, Nat. Commun. **6**, 7308 (2015).

[15] J. B. Varley, A. Miglio, V.-A. Ha, M. J. van Setten, G.-M. Rignanese, and G. Hautier, High-throughput design of non-oxide *p*-type transparent conducting materials: Data mining, search strategy, and identification of boron phosphide, Chem. Mater. **29**, 2568 (2017).

[16] R. K. M. Raghupathy, T. D. Kühne, C. Felser, and H. Mirhosseini, Rational design of transparent *p*-type conducting non-oxide materials from high-throughput calculations, J. Mater. Chem. C **6**, 541 (2018).

[17] R. K. M. Raghupathy, H. Wiebeler, T. D. Kühne, C. Felser, and H. Mirhosseini, Database screening of ternary chalcogenides for *p*-type transparent conductors, Chem. Mater. **30**, 6794 (2018).

[18] F. Ricci, W. Chen, U. Aydemir, G. J. Rey Snyder, G.-M. Rignanese, A. Jain, and G. Hautier, An *ab initio* electronic transport database for inorganic materials, Sci. Data **4**, 170085 (2017).

[19] Inorganic Crystal Structure Database, https://www.fiz-karlsruhe.de/de/leistungen/kristallographie/icsd.html.

[20] A. Jain, S. P. Ong, G. Hautier, W. Chen, W. D. Richards, S. Dacek, S. Cholia, D. Gunter, D. Skinner, G. Ceder, and K. A. Persson, The materials project: A materials genome approach to accelerating materials innovation, APL Mater. **1**, 011002 (2013).

[21] The Materials Project, https://www.materialsproject.org.

[22] G. Kresse and J. Furthmüller, Efficiency of *ab-initio* total energy calculations for metals and semiconductors using a plane-wave basis set, Comput. Mater. Sci. **6**, 15 (1996).

[23] G. Kresse and J. Furthmüller, Efficient iterative schemes for *ab initio* total-energy calculations using a plane-wave basis set, Phys. Rev. B **54**, 11169 (1996).

[24] J. P. Perdew, K. Burke, and M. Ernzerhof, Generalized Gradient Approximation Made Simple, Phys. Rev. Lett. **77**, 3865 (1996).

[25] P. E. Blöchl, Projector augmented-wave method, Phys. Rev. B **50**, 17953 (1994).

[26] J. Heyd, G. E. Scuseria, and M. Ernzerhof, Hybrid functionals based on a screened Coulomb potential, J. Chem. Phys. **118**, 8207 (2003).

[27] E. N. Brothers, A. F. Izmaylov, J. O. Normand, V. Barone, and G. E. Scuseria, Accurate solid-state band gaps via screened hybrid electronic structure calculations, J. Chem. Phys. **129**, 011102 (2008).

[28] X. Gonze, J.-M. Beuken, R. Caracas, F. Detraux, M. Fuchs, G.-M. Rignanese, L. Sindic, M. Verstraete, G. Zerah, F. Jollet, M. Torrent, A. Roy, M. Mikami, Ph. Ghosez, J.-Y. Raty, and D. C. Allan, First-principles computation of material properties: The ABINIT software project, Comput. Mater. Sci. **25**, 478 (2002).

[29] X. Gonze, A brief introduction to the ABINIT software package, Z. Kristallogr. **220**, 558 (2005).

[30] X. Gonze, B. Amadon, P.-M. Anglade, J.-M. Beuken, F. Bottin, P. Boulanger, F. Bruneval, D. Caliste, R. Caracas, M. Côté, T. Deutsch, L. Genovese, Ph. Ghosez, M. Giantomassi, S. Goedecker, D. R. Hamann, P. Hermet, F. Jollet, G. Jomard, S. Leroux, M. Mancini, S. Mazevet, M. J. T. Oliveira, G. Onida, Y. Pouillon, T. Rangel, G.-M. Rignanese, D. Sangalli, R. Shaltaf, M. Torrent, M. J. Verstraete, G. Zerah, and J. W. Zwanziger, ABINIT: First-principles approach of materials and nanosystem properties, Comput. Phys. Commun. **180**, 2582 (2009).

[31] X. Gonze, F. Jollet, F. Abreu Araujo, D. Adams, B. Amadon, T. Applencourt, C. Audouze, J.-M. Beuken, J. Bieder, A. Bokhanchuk, E. Bousquet, F. Bruneval, D. Caliste, M. Côté, F. Dahm, F. Da Pieve, M. Delaveau, M. Di Gennaro, B. Dorado, C. Espejo, G. Geneste, L. Genovese, A. Gerossier, M. Giantomassi, Y. Gillet, D. R. Hamann, L. He, G. Jomard, J. Laflamme Janssen, S. Le Roux, A. Levitt, A. Lherbier, F. Liu, I. Lukačević, A. Martin, C. Martins, M. J. T. Oliveira, S. Poncé, Y. Pouillon, T. Rangel, G.-M. Rignanese, A. H. Romero, B. Rousseau, O. Rubel, A. A. Shukri, M. Stankovski, M. Torrent, M. J. Van Setten, B. Van Troeye, M. J. Verstraete, D. Waroquiers, J. Wiktor, B. Xu, A. Zhou, and J. W. Zwanziger, Recent developments in the ABINIT software package, Comput. Phys. Commun. **205**, 106 (2016).

[32] D. R. Hamann, Optimized norm-conserving Vanderbilt pseudopotentials, Phys. Rev. B **88**, 085117 (2013).

[33] M. J. van Setten, M. Giantomassi, E. Bousquet, M. J. Verstraete, D. R. Hamann, X. Gonze, and G.-M. Rignanese, The pseudodojo: Training and grading an 85 element optimized norm-conserving pseudopotential table, Comput. Phys. Commun. **226**, 39 (2018).

[34] M. J. van Setten, M. Giantomassi, X. Gonze, G.-M. Rignanese, and G. Hautier, Automation methodologies and large-scale validation for *GW*: Towards high-throughput *GW* calculations, Phys. Rev. B **96**, 155207 (2017).

[35] S. P. Ong, W. D. Richards, A. Jain, G. Hautier, M. Kocher, S. Cholia, D. Gunter, V. L. Chevrier, K. A. Persson, and G. Ceder, PYTHON materials genomics (PYMATGEN): A robust, open-source PYTHON library for materials analysis, Comput. Mater. Sci. **68**, 314 (2013).

[36] M. Giantomassi *et al.*, Open-source library for analyzing the results produced by ABINIT, https://github.com/abinit/abipy.

[37] C. Freysoldt, B. Grabowski, T. Hickel, J. Neugebauer, G. Kresse, A. Janotti, and C. G. Van de Walle, First-principles

calculations for point defects in solids, Rev. Mod. Phys. **86**, 253 (2014).

[38] H.-P. Komsa, T. T. Rantala, and A. Pasquarello, Finite-size supercell correction schemes for charged defect calculations, Phys. Rev. B **86**, 045112 (2012).

[39] S. B. Zhang and J. E. Northrup, Chemical Potential Dependence of Defect Formation Energies in GaAs: Application to Ga Self-Diffusion, Phys. Rev. Lett. **67**, 2339 (1991).

[40] C. Freysoldt, J. Neugebauer, and C. G. Van de Walle, Electrostatic interactions between charged defects in supercells, Phys. Status Solidi B **248**, 1067 (2011).

[41] Y. Kumagai and F. Oba, Electrostatics-based finite-size corrections for first-principles point defect calculations, Phys. Rev. B **89**, 195205 (2014).

[42] D. Broberg, B. Medasani, N. E. R. Zimmermann, G. Yu, A. Canning, M. Haranczyk, M. Asta, and G. Hautier, PYCDT: A PYTHON toolkit for modeling point defects in semiconductors and insulators, Comput. Phys. Commun. **226**, 165 (2018).

[43] G. K. H. Madsen and D. J. Singh, BOLTZTRAP: A code for calculating band-structure dependent quantities, Comput. Phys. Commun. **175**, 67 (2006).

[44] A. Jain, S. P. Ong, W. Chen, B. Medasani, X. Qu, M. Kocher, M. Brafman, G. Petretto, G.-M. Rignanese, G. Hautier, D. Gunter, and K. A. Persson, Fireworks: A dynamic workflow system designed for high-throughput applications, Concurr. Comput. Pract. Exp. **27**, 5037 (2015).

[45] J. Noffsinger, F. Giustino, B. D. Malone, C.-H. Park, S. G. Louie, and M. L. Cohen, EPW: A program for calculating the electron-phonon coupling using maximally localized Wannier functions, Comput. Phys. Commun. **181**, 2140 (2010).

[46] S. Poncé, E. R. Margine, C. Verdi, and F. Giustino, EPW: Electron-phonon coupling, transport and superconducting properties using maximally localized Wannier functions, Comput. Phys. Commun. **209**, 116 (2016).

[47] P. Giannozzi, S. Baroni, N. Bonini, M. Calandra, R. Car, C. Cavazzoni, D. Ceresoli, G. L Chiarotti, M. Cococcioni, I. Dabo, A. Dal Corso, S. de Gironcoli, S. Fabris, G. Fratesi, R. Gebauer, U. Gerstmann, C. Gougoussis, A. Kokalj, M. Lazzeri, L. Martin-Samos, N. Marzari, F. Mauri, R. Mazzarello, S. Paolini, A. Pasquarello, L. Paulatto, C. Sbraccia, S. Scandolo, G. Sclauzero, A. P Seitsonen, A. Smogunov, P. Umari, and R. M Wentzcovitch, QUANTUM ESPRESSO: A modular and open-source software project for quantum simulations of materials, J. Phys.: Condens. Matter **21**, 395502 (2009).

[48] P. Giannozzi, O. Andreussi, T. Brumme, O. Bunau, M. Buongiorno Nardelli, M. Calandra, R. Car, C. Cavazzoni, D. Ceresoli, M. Cococcioni, N. Colonna, I. Carnimeo, A. Dal Corso, S. de Gironcoli, P. Delugas, R. A. DiStasio, A. Ferretti, A. Floris, G. Fratesi, G. Fugallo, R. Gebauer, U. Gerstmann, F. Giustino, T. Gorni, J. Jia, M. Kawamura, H.-Y. Ko, A. Kokalj, E. Küçükbenli, M. Lazzeri, M. Marsili, N. Marzari, F. Mauri, N. L. Nguyen, H.-V. Nguyen, A. Otero de-la Roza, L. Paulatto, S. Poncé, D. Rocca, R. Sabatini, B. Santra, M. Schlipf, A. P. Seitsonen, A. Smogunov, I. Timrov, T. Thonhauser, P. Umari, N. Vast, X. Wu, and S. Baroni, Advanced capabilities for materials modeling with QUANTUM ESPRESSO, J. Phys.: Condens. Matter **29**, 465901 (2017).

[49] M. Giantomassi, Core-electrons and self-consistency in the *GW* approximation from a PAW perspective, Ph.D. thesis, Université catholique de Louvain, 2009, Chap. 5 and Appendix B.

[50] G. Hautier, S. P. Ong, A. Jain, C. J. Moore, and G. Ceder, Accuracy of density functional theory in predicting formation energies of ternary oxides from binary oxides and its implication on phase stability, Phys. Rev. B **85**, 155208 (2012).

[51] See Supplemental Material at http://link.aps.org/supplemental/10.1103/PhysRevMaterials.3.034601 for more information about computational details and results.

[52] K. Furukawa, A. Uemoto, M. Shigeta, A. Suzuki, and S. Nakajima, 3C-SiC *p-n* junction diodes, Appl. Phys. Lett. **48**, 1536 (1986).

[53] Y. Kondo, T. Takahashi, K. Ishii, Y. Hayashi, E. Sakuma, S. Misawa, H. Daimon, M. Yamanaka, and S. Yoshida, Experimental 3C-SiC MOSFET, IEEE Electron Device Lett. **7**, 404 (1986).

[54] K. Shibahara, N. Kuroda, S. Nishino, and H. Matsunami, Fabrication of *p-n* junction diodes using homoepitaxially grown 6H-SiC at low temperature by chemical vapor deposition, Jpn. J. Appl. Phys. **26**, 1815 (1987).

[55] R. Weingärtner, P. J. Wellmann, M. Bickermann, D. Hofmann, T. L. Straubinger, and A. Winnacker, Determination of charge carrier concentration in *n*- and *p*-doped SiC based on optical absorption measurements, Appl. Phys. Lett. **80**, 70 (2002).

[56] W. J. Choyke and G. Pensl, Physical properties of SiC, MRS Bull. **22**, 25 (1997).

[57] H. Morkoç, S. Strite, G. B. Gao, M. E. Lin, B. Sverdlov, and M. Burns, Large-band-gap SiC, III-V nitride, and II-VI ZnSe-based semiconductor device technologies, J. Appl. Phys. **76**, 1363 (1994).

[58] H. R. Philipp, Intrinsic optical absorption in single-crystal silicon carbide, Phys. Rev. **111**, 440 (1958).

[59] M. Liu, M. B. Johnston, and H. J. Snaith, Efficient planar heterojunction perovskite solar cells by vapour deposition, Nature (London) **501**, 395 (2013).

[60] M. A. Green, A. Ho-Baillie, and H. J. Snaith, The emergence of perovskite solar cells, Nat. Photonics **8**, 506 (2014).

[61] V.-A. Ha, F. Ricci, G.-M. Rignanese, and G. Hautier, Structural design principles for low hole effective mass *s*-orbital-based *p*-type oxides, J. Mater. Chem. C **5**, 5772 (2017).

[62] G. A. Saum and E. B. Hensley, Fundamental optical absorption in the IIa-VIb compounds, Phys. Rev. **113**, 1019 (1959).

[63] T. J. Richardson, New electrochromic mirror systems, Solid State Ionics **165**, 305 (2003).

[64] R. Gobrecht, Photoelektrische eigenschaften von lithiumantimonid, Phys. Status Solidi **13**, 429 (1966).

[65] J. Noffsinger, E. Kioupakis, C. G. Van de Walle, S. G. Louie, and M. L. Cohen, Phonon-Assisted Optical Absorption in Silicon from First Principles, Phys. Rev. Lett. **108**, 167402 (2012).

[66] N. F. Quackenbush, J. P. Allen, D. O. Scanlon, S. Sallis, J. A. Hewlett, A. S. Nandur, B. Chen, K. E. Smith, C. Weiland, D. A. Fischer, J. C. Woicik, B. E. White, G. W. Watson, and L. F. J. Piper, Origin of the bipolar doping behavior of SnO from x-ray spectroscopy and density functional theory, Chem. Mater. **25**, 3114 (2013).

[67] G. Hautier, A. Miglio, D. Waroquiers, G.-M. Rignanese, and X. Gonze, How does chemistry influence electron effective mass in oxides? A high-throughput computational analysis, Chem. Mater. **26**, 5447 (2014).

[68] K. Kuhar, M. Pandey, K. S. Thygesen, and K. W. Jacobsen, High-throughput computational assessment of previously synthesized semiconductors for photovoltaic and photoelectrochemical devices, ACS Energy Lett. **3**, 436 (2018).

[69] J. Tate, H. L. Ju, J. C. Moon, A. Zakutayev, A. P. Richard, J. Russell, and D. H. McIntyre, Origin of *p*-type conduction in single-crystal $CuAlO_2$, Phys. Rev. B **80**, 165206 (2009).

[70] Y. Ogo, H. Hiramatsu, K. Nomura, H. Yanagi, T. Kamiya, M. Hirano, and H. Hosono, *p*-channel thin-film transistor using *p*-type oxide semiconductor, SnO, Appl. Phys. Lett. **93**, 032113 (2008).

[71] E. Maciá-Barber, *Thermoelectric Materials: Advances and Applications* (Pan Stanford, Florida, USA, 2015).

[72] T. Kajikawa, N. Kimura, and T. Yokoyama, Thermoelectric properties of intermetallic compounds: Mg_3Bi_2 and Mg_3Sb_2 for medium temperature range thermoelectric elements, in *Proceedings ICT'03: 22nd International Conference on Thermoelectrics* (IEEE, New Jersey, USA, 2003).

[73] C. L. Condron, S. M. Kauzlarich, F. Gascoin, and G. J. Snyder, Thermoelectric properties and microstructure of Mg_3Sb_2, J. Solid State Chem. **179**, 2252 (2006).

[74] J. Zhang, L. Song, A. Mamakhel, M. R. V. Jørgensen, and B. B. Iversen, High-performance low-cost *n*-type Se-doped Mg_3Sb_2-based Zintl compounds for thermoelectric application, Chem. Mater. **29**, 5371 (2017).

[75] A. Zunger, Practical doping principles, Appl. Phys. Lett. **83**, 57 (2003).